APL Photonics

Fiber-integrated hollow-core light cage for gas spectroscopy

Cite as: APL Photonics **6**, 061301 (2021); https://doi.org/10.1063/5.0048501
Submitted: 23 February 2021 • Accepted: 18 May 2021 • Published Online: 07 June 2021

Bumjoon Jang, Julian Gargiulo, Jisoo Kim, et al.

Fiber-integrated hollow-core light cage for gas spectroscopy

Cite as: APL Photon. 6, 061301 (2021); doi: 10.1063/5.0048501
Submitted: 23 February 2021 • Accepted: 18 May 2021 •
Published Online: 7 June 2021

Bumjoon Jang,[1,2] Julian Gargiulo,[3] Jisoo Kim,[1,2] Johannes Bürger,[3] Steffen Both,[4] Hartmut Lehmann,[1] Torsten Wieduwilt,[1] Thomas Weiss,[4] Stefan A. Maier,[3,5] and Markus A. Schmidt[1,2,6,a)]

AFFILIATIONS

[1] Leibniz Institute of Photonic Technology, Albert-Einstein-Str. 9, 07745 Jena, Germany
[2] Abbe Center of Photonics and Faculty of Physics, Friedrich-Schiller-Universität Jena, Max-Wien-Platz 1, 07743 Jena, Germany
[3] Chair in Hybrid Nanosystems, Nanoinstitute Munich, Ludwig-Maximilians-Universität Munich, Königinstrasse 10, 80539 Munich, Germany
[4] 4th Physics Institute and Research Center SCoPE, University of Stuttgart, Pfaffenwaldring 57, 70569 Stuttgart, Germany
[5] The Blackett Laboratory, Department of Physics, Imperial College London, London SW7 2AZ, United Kingdom
[6] Otto Schott Institute of Materials Research (OSIM), Friedrich-Schiller-Universität Jena, Fraunhoferstr. 6, 07743 Jena, Germany

[a)] **Author to whom correspondence should be addressed:** markus-alexander.schmidt@uni-jena.de

ABSTRACT

Interfacing integrated on-chip waveguides with spectroscopic approaches represents one research direction within current photonics aiming at reducing geometric footprints and increasing device densities. Particularly relevant is to connect chip-integrated waveguides with established fiber-based circuitry, opening up the possibility for a new class of devices within the field of integrated photonics. Here, one attractive waveguide is the on-chip light cage, confining and guiding light in a low-index core through the anti-resonance effect. This waveguide, implemented via 3D nanoprinting and reaching nearly 100% overlap of mode and material of interest, uniquely provides side-wise access to the core region through the open spaces between the cage strands, drastically reducing gas diffusion times. Here, we extend the capabilities of the light cage concept by interfacing light cages and optical fibers, reaching a fully fiber-integrated on-chip waveguide arrangement with its spectroscopic capabilities demonstrated here on the example of tunable diode laser absorption spectroscopy of ammonia. Controlling and optimizing the fiber circuitry integration have been achieved via automatic alignment in etched v-grooves on silicon chips. This successful device integration via 3D nanoprinting highlights the fiber-interfaced light cage to be an attractive waveguide platform for a multitude of spectroscopy-related fields, including bio-analytics, lab-on-chip photonic sensing, chemistry, and quantum metrology.

I. INTRODUCTION

Sensing of gases is important for many areas of science and technology, such as pollution monitoring in environmental research[1] or breath analysis in life science.[2] In general, gases can be detected by using sensors based on different techniques, examples of which include semiconducting metal oxide sensors,[3–5] catalytic sensors,[6] and optical sensors.[7]

One highly relevant approach is tunable diode laser absorption spectroscopy (TDLAS), a widely used optical sensing technique that can achieve fast, selective, and reliable sensing of trace gases via spectroscopic detection of molecular fingerprints.[8–10] The sensitivity of TDLAS can be enhanced by integrated waveguides, providing significantly longer light–matter interaction lengths compared to free-space configurations.

From the perspective of fiber optics, microstructured optical fibers (MOFs) and post-processed fibers have been employed for gas sensing in chemical and biological applications,[11–14] while recently hollow-core-type MOFs have gained substantial attraction due to simplified fabrication.[15,16] Gas sensing applications have successfully been demonstrated in hollow-core MOFs, such as Kagomé-type fibers[17] and photonic bandgap fibers,[18–20] with near 100% spatial

overlap between light and gas, allowing for the direct use of the Lambert–Beer law without the knowledge of the modal fields. The majority of planar waveguides employed for gas sensing rely on interaction of the gas with evanescent fields, examples of which include silicon-on-insulator (SOI) waveguides,[21] slot waveguides,[22] ring resonators,[23,24] silicon–nitride waveguides,[25] and plasmonic Mach–Zehnder interferometers.[26] Recently, hollow-core antiresonant reflecting optical waveguides (ARROWs) have also been used for sensing atomic vapor.[27]

Although being successfully employed, fibers and, in particular, planar waveguides can show limitations with respect to gas sensing: the complexity in MOF drawing and electron-beam lithography makes them not straightforward for cost-efficient prototyping. Moreover, SOI and slot waveguides show limited overlap between electromagnetic fields and the ensemble of gas molecules due to the use of evanescent fields, while efficient interfacing of such waveguides to fiber circuitry remains a challenging research task. In the case of hollow-core-type structures, MOFs and planar waveguides are laterally sealed along the light guiding axis, i.e., encapsulating a central core region, thus relying on the openings at the waveguide's ends for gas filling. This can lead to exceedingly long filling times, particularly in situations relying on diffusion. For instance, the filling of low-pressure alkali vapor into a centimeters-long hollow-core fiber can take months to reach sufficient molecule concentrations.[28]

To address these limitations, the light guidance mechanism of hollow-core fibers has been merged with chip-based technology by establishing a new type of 3D nano-printed hollow-core waveguide—the light cage [shown in Figs. 1(d) and 1(e)][29,30]—guiding the light in the central hollow section across centimeter distances via the anti-resonance effect.[29,31] The structure consists of a sparse hexagonal array of micrometers-diameter cylindrical strands surrounding a central hollow core. The maximum length of the light cage achieved so far is 3 cm, yielding single-strand aspect ratios as high as 8300.[37] Specific features of the light cage concept relevant within the context of absorption spectroscopy are (i) close-to-unity overlap of the electromagnetic field with the core material, (ii) diffraction-less guidance over centimeter distances,

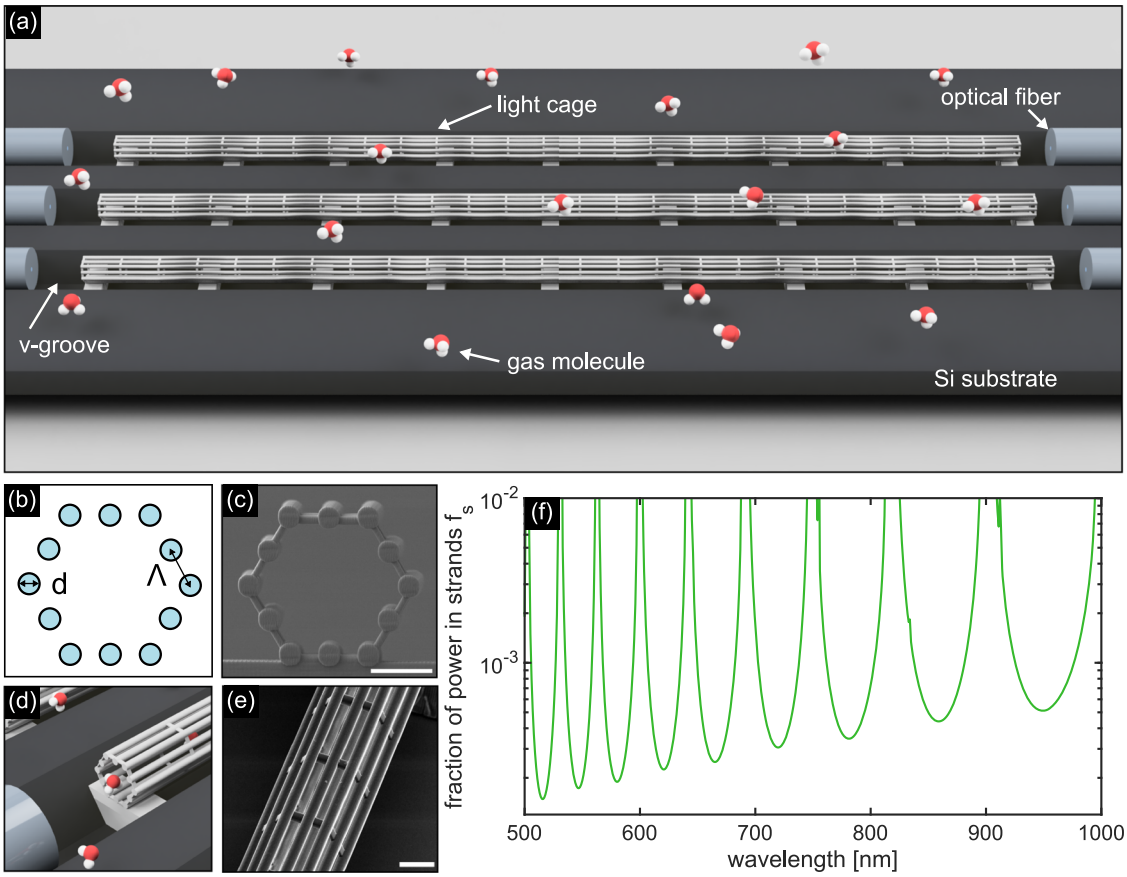

FIG. 1. Fiber-connected light cage on chip as a gas sensing platform. (a) Schematic of the fiber-connected light cage, which consists of in-/out-coupling optical fibers fixed on a v-groove and 3D printed light cage. The molecules are not to scale. (b) Cross-sectional diagram of the light cage, d is the diameter of polymer strands, and Λ is the pitch, center-to-center distance between the strands. (c) Scanning electron microscopic (SEM) image of the light cage. (d) Zoomed-in angle view of the schematic showing the edge coupling configuration of the optical fiber and light cage. (e) Angle view of the SEM image showing the cage structure. (f) Dispersion of f_s, the fraction of power in the strands that does not contribute to the interaction with gas. Scale bars are 10 μm.

and (iii) side-wise access to the core region, which was used for, e.g., absorption spectroscopic experiments in an aqueous environment.[32] Note that the employment of direct laser writing (DLW) via two-photon polymerization enables fast prototyping (~1 cm light cage per hour), which is essential for the optimization of waveguide designs in contrast to fiber-drawing that typically demands much longer time for implementation. Moreover, DLW allows for the realization of complex geometries that are neither possible with planar technology nor using fiber-drawing to efficiently interface light cages to this circuitry.

The latter point represents a long standing challenge of planar waveguide technology, which is to realize efficient fiber-to-chip and chip-to-chip configurations. For most photonic chip devices, either grating coupling or edge coupling is used for launching light into and collecting it from photonic circuitry.[33] However, grating couplers require optical fibers to be placed outside of the chip at a certain angle usually demanding special mounting. Edge coupling of planar waveguides requires particular technical conditions, such as near sub-micrometer precision alignment for optimal coupling[34] and high quality polishing of planar waveguide end faces.[35] In this Letter, we demonstrate the successful interfacing of light cages with fiber circuitry and in-line ammonia gas sensing using TDLAS at the near infrared (NIR) wavelength [Figs. 1(a) and 1(d)]. In contrast to free-space coupling with bulk optics, the optical coupling between light cage and in/output fibers on a single chip makes the device portable and highly relevant, particularly from the perspective of applications within, for instance, the lab-on-chip photonic sensing community.

The light cage geometry used in this work is composed of twelve cylindrical strands [diameter $d = 3.6\,\mu$m in Fig. 1(b) and inter-strand center-to-center spacing (pitch) $\Lambda = 7\,\mu$m], forming a hexagonal air core in a triangular lattice. In analogy to hollow-core fibers, guidance inside light cages is provided by means of anti-resonance and inhibited coupling effects,[36] leading to the formation of leaky modes inside the core section.[29] This interference effect imposes a characteristic spectral evolution of transmission. The transmission spectrum consists of regions of broad high-transmission bands and narrow lossy resonances with strong modal attenuation. As shown in Refs. 29 and 37, light cages show losses of the order of 0.1, . . ., 1 dB/mm in the visible spectral domain, suggesting a similar loss level at telecommunication wavelengths. Recently, we have revealed that via the current implementation strategy, the maximum feasible light cage length is 3 cm as demonstrated experimentally.[37] Particularly important within the context of absorption spectroscopy and device including one or more absorptive materials (e.g., plasmonics in fibers[38]) is the fraction of the field interacting with the material of interest. For light cages, this is correlated with the fraction of power in the strands,[32] f_s, which has been calculated here by the multipole expansion method,[39,40] followed by analytic mode normalization for leaky modes.[41–43] The refractive index of the polymer is described in Ref. 30, and the background material was set as air ($n_{\text{air}} = 1$). As shown in Fig. 1(f), f_s is below $< 10^{-3}$ outside the narrow spectral regions that correspond to the resonance domains. This fact suggests that almost all the electromagnetic power is available for spectroscopy, allowing the direct application of the Beer–Lambert law in its unmodified form[44]

$$A = \log_{10}(P_0/P) = \varepsilon c l. \tag{1}$$

Here, A is the (decadic) absorbance, P_0 is the incident power, P is the transmitted power, ε is the molecular absorption coefficient, c is the concentration, and l is the absorption path length. The direct use of Eq. (1)—an issue that was also observed for light cages immersed in water[32]—represents an essential difference to evanescent-field-based sensing schemes.[45,46] The evanescent field yields non-negligible f_s-values ($0.2 < f_s < 0.5$) requiring the inclusion of f_s to the Beer–Lambert law and, therefore, demanding additional mode calculations. The small values of f_s in the case of the light cage are remarkable, given the fact that the cage is side-wise open and the strands cover only 4% of the entire light cage area.

The fiber-connected light cage chip is shown schematically in Fig. 1(a). Note that the strand array (a light cage length of 5 mm) is mechanically supported by reinforcement rings every 45 μm [Fig. 1(e)] in order to prevent structural collapsing during development. Due to the small geometric footprint, multiple light cages can be integrated on a single chip [Fig. 1(a)]. Highly reproducible direct fiber-to-light cage coupling [Fig. 1(d)] has been achieved by self-aligning of light cages and fibers via v-grooves anisotropically etched into the silicon chips, thus avoiding expensive alignment techniques requiring very high precision.[33] The alignment precision relies on the high accuracy of the angle of v-shape, which is determined here to a very high precision by the crystalline structure of silicon [54.7°, between the (111) facet and the (001) surface of silicon]. Here, the role of the v-grooves is to mechanically fix the in- and output fibers in a well-defined position with respect to each other and the light cage. Both fibers were fixed inside the v-grooves by UV curing epoxy (Vitralit® 1605) and a glass lid, leaving an empty space of ~5 mm between them for printing light cages. One chip typically contains three to five v-grooves, while there is no principal limitation to increase that number further. The permanent fixation of the fibers within the v-grooves leads to stable operation with no variations of the output signal over time.

Fiber-connected light cages were fabricated using a Nanoscribe direct laser writing system (Photonics Professional GT, Nanoscribe GmbH). A silicon chip with fibers attached on v-grooves was mounted on the sample holder with grooves aligned horizontally. The quality of alignment between the grooves and the axis of the Nanoscribe system was monitored on site using a 20× air objective. The distance between the light cage and in- and out-coupling fibers, s_{in} [depicted in Fig. 2(a)] and s_{out}, was used to calculate the length and position of the light cage in the coordinate system in Nanoscribe printing software (DeScribe, Nanoscribe GmbH). The light cages were printed in immersion configuration with a liquid negative-tone two-photon polymerization resin (IP-DIP, Nanoscribe GmbH) and a 63× objective. The detailed printing strategy of light cage components is described elsewhere.[29,30] A custom-made code written in NanoWrite (Nanoscribe GmbH) was used to control the shape of each element of the light cage, allowing for accurately aligning them to the fibers.

Optimization of coupling conditions has been achieved here via adjusting the distance between the in-coupling fiber and the light cage s_{in}. To optimize both transmission properties and mode excitation simultaneously, single-mode (SM) fibers (SM600, Fibercore, cutoff wavelength: 550 nm) were attached only on the input side of the chip to allow for measuring the mode pattern [see the inset of Fig. 2(b)]. After launching white light (SuperK COMPACT, NKT Photonics) to the delivery fiber, mode images were taken at different

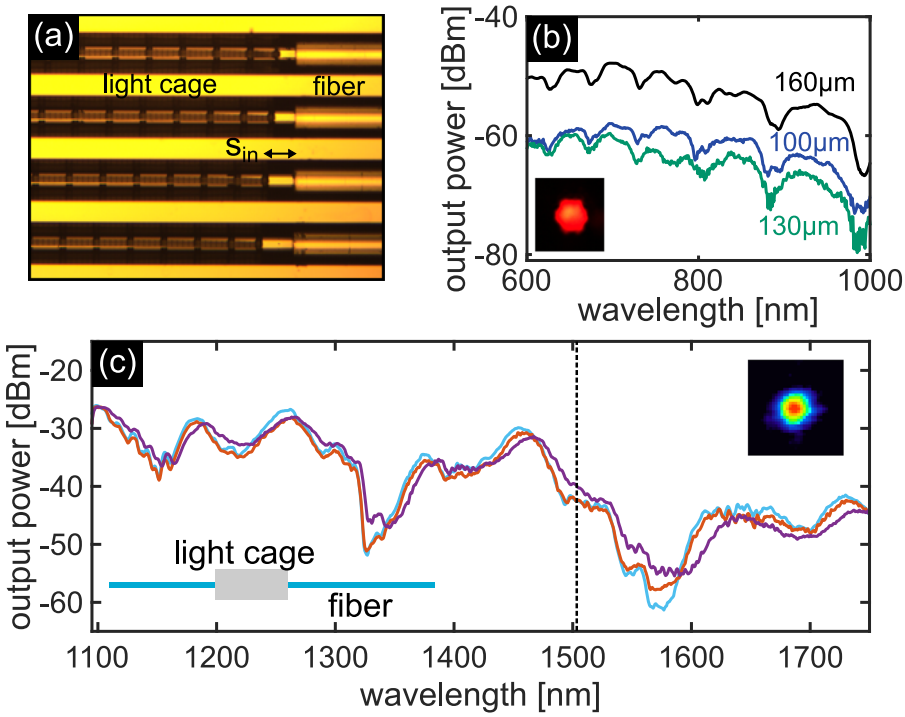

FIG. 2. Transmission experiment with the fiber-connected light cage. (a) Micrograph of the light cages interfacing with single-mode fibers (visible range) on v-grooves, while the distance between them (s_{in}) is varied between grooves. (b) Transmission spectrum of the sample shown in (a). Plotted curves represent grooves with different s_{in} (indicated adjacent to the curves). This sample has fibers connected only on one side to investigate the coupling efficiency. The inset is a mode image at 633 nm (s_{in} = 160 μm), showing the hexagonal core of the light cage. (c) Transmission spectrum of a fiber-connected light cage for NIR. Three curves were measured from different grooves with constant s_{in} = 160 μm, showing high reproducibility of the fabrication. The vertical dashed line indicates the target wavelength (1501 nm) of ammonia sensing. The bottom-left inset shows a diagram of the fiber-connected light cage. The top-right inset shows a mode image of the single-sided version of the NIR sample.

wavelengths using a bandpass filter. The coupling efficiency between the delivery fiber and the light cage was determined by measuring the output power in the presence and absence of a single-side interfaced light cage (for details, see the supplementary material). Assuming a propagation loss of 1 dB/mm as reported in previous works,[29,37] the coupling efficiency was determined to be 0.87. This value agrees with those obtained by integrating the mode overlap of the light cage and the diffractive output beam of the fiber at different distances s_{in}. Here, for the two SMFs (single-mode fibers) [SM600 (Fibercore) and SMF28 (Thorlabs)] used in this work, $50 < s_{in} < 170\,\mu$m yields efficiency higher than 80%, while the optimal distance is close to 100 μm. Note that the delivery fibers are chosen as such to support only a single mode in the spectral interval of interest, preventing the emergence of modal beat patterns in the transmission spectra. Figure 2(b) shows the transmission spectra of three v-grooves for different s_{in} (100, 130, and 160 μm). Whereas the two small distances (s_{in} = 100, 130 μm) show a comparably low transmission and small fringe (extinction contrast), the curve referring to s_{in} = 160 μm [the black curve in Fig. 2(a)] shows better coupling and a clearer fingerprint of anti-resonance guidance, i.e., a distinct alternating sequence of regions of high and low transmission. The low efficiency at shorter s_{in} might be explained by the shadowing effect from the fiber during writing, partially blocking the writing beam path and thus affecting the polymerization process, or from misalignment of the light cage and fiber (note that controlling implementation along the vertical directions is challenging). Therefore, the experimentally determined value of s_{in} = 160 μm was chosen for this work. Note that the mode image [see the inset of Fig. 2(b)] measured at λ = 633 nm clearly resembles the hexagonal shape of the light cage, thus confirming the efficient excitation of the fundamental core mode.

To reach a completely fiber-connected chip design that can be used for TDLAS at NIR wavelengths, v-groove chips containing SMF (SMF28, Thorlabs) for in-coupling and MMF (multi-mode fiber) (FG050LGA, Thorlabs) for out-coupling have been prepared. For the MMF, we chose a fiber with a large core (50 μm) and, according to the argumentation above, kept the distance between the light cage and MMF as s_{out} = 160 μm. The measured transmission spectra for three identically prepared light cages at the NIR wavelength on the same chip [Fig. 2(b)] show clear features of anti-resonance guidance similar to the visible spectral domain [Fig. 2(a)]. Note that the overlap of the three curves clearly highlights the high reproducibility of both light cages and fiber coupling configuration and suggests that the combination of fiber fixation via gluing and 3D nanoprinting represents a highly reproducible implementation scheme.

To demonstrate the capabilities of the fiber-coupled light cage with respect to TDLAS, we used the sample discussed in Fig. 2(c) for sensing ammonia. The target wavelength was chosen around 1501 nm [indicated by the vertical dashed line in Fig. 2(c)], matching the single-mode region of the SMF and lying in one high-transmission window of the device. Experimentally, the fiber-connected light cage was placed in a sealed gas flow cell that consists of in/out gas tubing connectors and two slits for the fibers [Fig. 3(a)]. To perform concentration sensitive measurements, defined compositions of ammonia and nitrogen were prepared in a gas mixer. The relative concentration of ammonia in nitrogen was fixed by using computer-controlled mass-flow meters. For the TDLAS measurements, a tunable external cavity diode laser (TUNICS 1550, Photonetics) was connected to a Y-fiber coupler through the use of FC/PC connectors, yielding highly reproducible coupling conditions. One arm was directed to a photodiode (S122C, Thorlabs) to monitor the

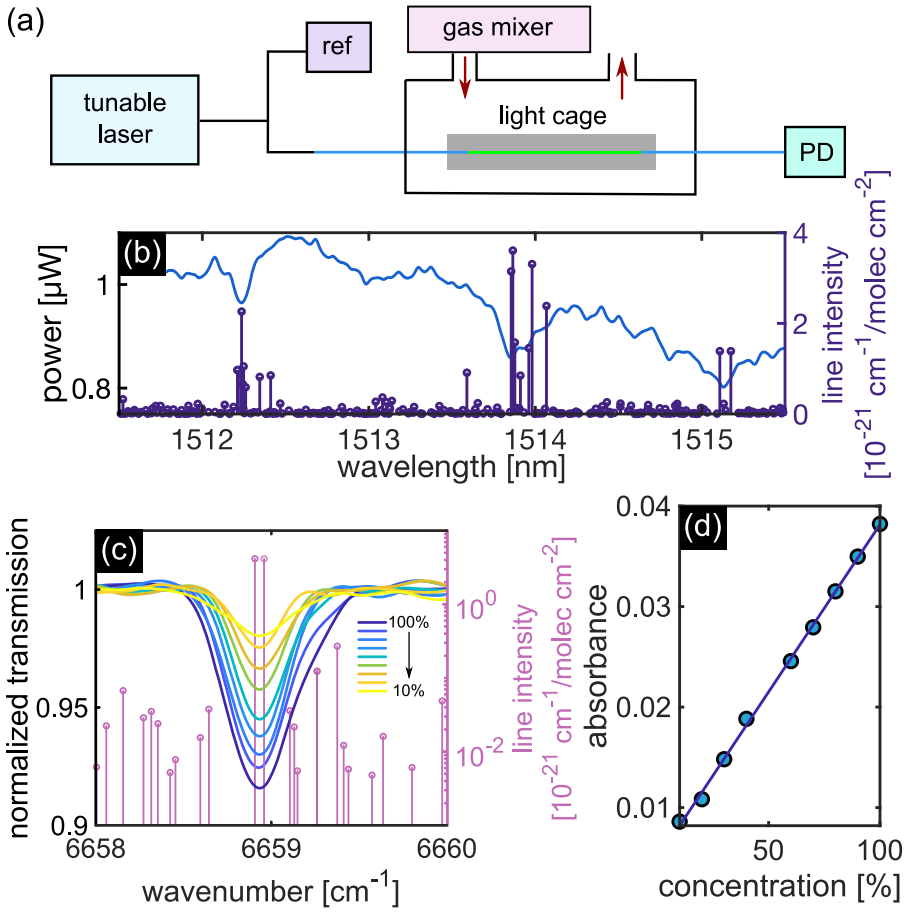

FIG. 3. Demonstration of ammonia absorption spectroscopy. (a) Diagram of the gas sensing setup. Tunable laser is connected to a Y-coupler, one leg to a reference photodiode and one connected to the in-coupling fiber of the light cage by using a fiber connector. The chip is placed in a gas chamber with the outlets connected to the gas mixer and exhaustion, respectively. The out-coupling fiber is connected to a photodiode (PD) (b) broad range ammonia absorption measurement. The blue curve represents the measured output power showing dips that match absorption lines from the HITRAN database[47] (plotted as purple bars). (c) Transmission at different concentrations of ammonia [values indicated in legend; circles: absorption lines of ammonia (HITRAN database)]. (d) Absorbance plotted and linearly fitted at the absorption line 1501.75 nm (wavenumber: 6658.9 cm^{-1}).

stability of the laser, while the other arm was butt-coupled to the SMF of the sample. The light transmitted through the light cage and collected by the MMF was fed to a photodiode power sensor (S155C, Thorlabs), with the transmitted power level being continuously recorded. During the TDLAS measurement, the wavelength of the laser was swept in 1 pm steps in the spectral region of interest. The total power throughput efficiency—the output power measured by the photodiode divided by the power that propagates inside the delivery fiber before coupled to the light cage—was ~5% (for details, see the supplementary material).

To verify the presence of ammonia, a broadband scan of ~4 nm wide was performed showing multiple strong absorption lines after flushing the gas chamber with ammonia. As shown in Fig. 3(b), the absorption spectrum (light blue curve) shows a good match with theoretical ammonia ($^{15}NH_3$) absorption data from the HITRAN database[47] (vertical purple bars). Note that the variations in transmitted power mainly result from fluctuations of the laser source (details can be found in the supplementary material). Figure 3(c) shows the result of the TDLAS measurement for various ammonia concentrations for a selected absorption line ($\nu_1 + \nu_3$) with λ = 1501.75 nm (wavenumber: 6658.9 cm^{-1}).[47] The concentration was changed every 5 min after measuring the spectrum twice at each concentration. Each measurement took ~2 min. Note that the time scale is determined by the speed of the tunable laser and gas mixer, not the filling time of the device. The output power was normalized to the individual measurement baseline outside the resonance that linearly connects the transmission values at the boundary of the spectral interval considered (6658 and 6660 cm^{-1}). As expected, higher concentrations lead to lower transmission values at the main absorption wavenumber. Note that through analyzing the absorption lines in the vicinity of the main line [dark circles in Fig. 3(c)], we found that the variations of the line shape at the highest ammonia concentrations (90% and 100%) on the high frequency side of the transmission dip can be attributed to additional absorption features that contribute in case the ammonia concentration exceeds a certain value. To quantify the concentration/absorption dependence and to obtain the limit of detection (LoD), the corresponding absorbance at the main absorption wavelength is plotted against ammonia concentration [Fig. 3(d)], showing a linear dependence ($A = 0.000\,333 \cdot c + 0.004\,867$, where c is the concentration) defining the calibration curve in accordance with Eq. (1).

According to the widely used concept of limit of detection (LoD) based on the 3-σ criterion ($LoD = 3 \cdot \sigma_A/\varepsilon l$), the smallest relative concentration that the current system can detect is around 3.37% (volume concentration). Since the slope of the calibration curve is inversely proportional to the interaction length, further

improvement of the sensitivity can be achieved by increasing the length of the light cage. For instance, if this length is increased to 3 cm (current fabrication limit), the LoD can be reduced to less than 1%. Using longer samples would also strongly improve the signal-to-noise ratio of the absorption lines shown in Fig. 3(b) (see the supplementary material for details).

II. CONCLUSION

Here, we introduced the concept of the fiber-interfaced light cages that combines the advantages of hollow-core light cages with commonly used optical fibers within a single device. Specifically, we demonstrated the integration of light cage sensing structures into a conventional fiber-based probing setup based on conventional optical fibers. Controlling and optimizing were achieved by automatic alignment inside v-grooves etched into silicon chips. The capabilities of this fiber-integrated system with respect to spectroscopic applications were demonstrated by integrated tunable diode laser absorption spectroscopy on the example of ammonia. Our concept constitutes the first demonstration of reliable on-chip usage of light cages, which should be of significant interest for the lab-on-chip photonic sensing community. By this successful device integration through 3D nanoprinting, we believe that the portability and flexibility of this approach and its potential for further integration with chip devices make fiber-connected light cages an attractive concept for applications in a multitude of fields, including bio-analytics, chemistry, and quantum metrology, all of which demand to confine an accessible and propagating optical mode within a waveguide architecture with small geometric footprint.

SUPPLEMENTARY MATERIAL

See the supplementary material for more details on transmission efficiencies, characterization of the scanning laser source, and contrast of absorption lines.

ACKNOWLEDGMENTS

This work was supported, in part, by the German Research Foundation (Grant Nos. MA 4699/2-1, WE 5815/5-1, SPP 1839, SCHM 2655/15-1, and SCHM 2655/8-1) and the Lee-Lucas Chair in Physics at Imperial College London. We also acknowledge the Open Access Publication Fund of the Thueringer Universitaets- und Landesbibliothek Jena (Projekt-Nr. 433052568).

DATA AVAILABILITY

The data that support the findings of this study are available from the corresponding author upon reasonable request.

REFERENCES

[1] P. Kumar, L. Morawska, C. Martani, G. Biskos, M. Neophytou, S. Di Sabatino, M. Bell, L. Norford, and R. Britter, "The rise of low-cost sensing for managing air pollution in cities," Environ. Int. **75**, 199–205 (2015).
[2] D. Yan, J. Popp, and T. Frosch, "Analysis of fiber-enhanced Raman gas sensing based on Raman chemical imaging," Anal. Chem. **89**, 12269–12275 (2017).
[3] C. Wang, L. Yin, L. Zhang, D. Xiang, and R. Gao, "Metal oxide gas sensors: Sensitivity and influencing factors," Sensors **10**, 2088–2106 (2010).
[4] M. Poloju, N. Jayababu, and M. V. Ramana Reddy, "Improved gas sensing performance of Al doped ZnO/CuO nanocomposite based ammonia gas sensor," Mater. Sci. Eng.: B **227**, 61–67 (2018).
[5] V. Kekkonen, S. Chaudhuri, F. Clarke, J. Kaisto, J. Liimatainen, S. K. Pandian, J. Piirto, M. Siltanen, and A. Zolotukhin, "Picosecond pulsed laser deposition of metal-oxide sensing layers with controllable porosity for gas sensor applications," Appl. Phys. A **122**, 233 (2016).
[6] A. Harley-Trochimczyk, T. Pham, J. Chang, E. Chen, M. A. Worsley, A. Zettl, W. Mickelson, and R. Maboudian, "Platinum nanoparticle loading of boron nitride aerogel and its use as a novel material for low-power catalytic gas sensing," Adv. Funct. Mater. **26**, 433–439 (2016).
[7] J. Hodgkinson and R. P. Tatam, "Optical gas sensing: A review," Meas. Sci. Technol. **24**, 012004 (2013).
[8] D. Brueckner, D. Roesti, U. G. Zuber, R. Schmidt, S. Kraehenbuehl, G. Bonkat, and O. Braissant, "Comparison of tunable diode laser absorption spectroscopy and isothermal micro-calorimetry for non-invasive detection of microbial growth in media fills," Sci. Rep. **6**, 27894 (2016).
[9] X. Guo, F. Zheng, C. Li, X. Yang, N. Li, S. Liu, J. Wei, X. Qiu, and Q. He, "A portable sensor for *in situ* measurement of ammonia based on near-infrared laser absorption spectroscopy," Opt. Lasers Eng. **115**, 243–248 (2019).
[10] L. Dong, F. K. Tittel, C. Li, N. P. Sanchez, H. Wu, C. Zheng, Y. Yu, A. Sampaolo, and R. J. Griffin, "Compact TDLAS based sensor design using interband cascade lasers for mid-IR trace gas sensing," Opt. Express **24**, A528 (2016).
[11] A. M. Cubillas, S. Unterkofler, T. G. Euser, B. J. M. Etzold, A. C. Jones, P. J. Sadler, P. Wasserscheid, and P. S. J. Russell, "Photonic crystal fibres for chemical sensing and photochemistry," Chem. Soc. Rev. **42**, 8629–8648 (2013).
[12] N. L. P. Andrews, R. Ross, D. Munzke, C. van Hoorn, A. Brzezinski, J. A. Barnes, O. Reich, and H.-P. Loock, "In-fiber Mach–Zehnder interferometer for gas refractive index measurements based on a hollow-core photonic crystal fiber," Opt. Express **24**, 14086 (2016).
[13] X. Feng, W. Feng, C. Tao, D. Deng, X. Qin, and R. Chen, "Hydrogen sulfide gas sensor based on graphene-coated tapered photonic crystal fiber interferometer," Sens. Actuators, B **247**, 540–545 (2017).
[14] P. Hu, X. Dong, W. C. Wong, L. H. Chen, K. Ni, and C. C. Chan, "Photonic crystal fiber interferometric pH sensor based on polyvinyl alcohol/polyacrylic acid hydrogel coating," Appl. Opt. **54**, 2647 (2015).
[15] A. Hartung, J. Kobelke, A. Schwuchow, J. Bierlich, J. Popp, M. A. Schmidt, and T. Frosch, "Low-loss single-mode guidance in large-core antiresonant hollow-core fibers," Opt. Lett. **40**, 3432 (2015).
[16] Y. Y. Wang, N. V. Wheeler, F. Couny, P. J. Roberts, and F. Benabid, "Low loss broadband transmission in hypocycloid-core Kagome hollow-core photonic crystal fiber," Opt. Lett. **36**, 669 (2011).
[17] F. Benabid, J. C. Knight, G. Antonopoulos, and P. S. J. Russell, "Stimulated Raman scattering in hydrogen-filled hollow-core photonic crystal fiber," Science **298**, 399–402 (2002).
[18] F. Yang, W. Jin, Y. Cao, H. L. Ho, and Y. Wang, "Towards high sensitivity gas detection with hollow-core photonic bandgap fibers," Opt. Express **22**, 24894 (2014).
[19] N. V. Wheeler, A. M. Heidt, N. K. Baddela, E. N. Fokoua, J. R. Hayes, S. R. Sandoghchi, F. Poletti, M. N. Petrovich, and D. J. Richardson, "Low-loss and low-bend-sensitivity mid-infrared guidance in a hollow-core–photonic-bandgap fiber," Opt. Lett. **39**, 295 (2014).
[20] W. Jin, Y. Cao, F. Yang, and H. L. Ho, "Ultra-sensitive all-fibre photothermal spectroscopy with large dynamic range," Nat. Commun. **6**, 6767 (2015).
[21] L. Tombez, E. J. Zhang, J. S. Orcutt, S. Kamlapurkar, and W. M. J. Green, "Methane absorption spectroscopy on a silicon photonic chip," Optica **4**, 1322–1325 (2017).
[22] Y. Zou, H. Subbaraman, S. Chakravarty, X. Xu, A. Hosseini, W.-C. Lai, P. Wray, and R. T. Chen, "Grating-coupled silicon-on-sapphire integrated slot waveguides operating at mid-infrared wavelengths," Opt. Lett. **39**, 3070 (2014).
[23] J. T. Robinson, L. Chen, and M. Lipson, "On-chip gas detection in silicon optical microcavities," Opt. Express **16**, 4296 (2008).
[24] S. Zou, F. Wang, R. Liang, L. Xiao, and M. Hu, "A nanoscale refractive index sensor based on asymmetric plasmonic waveguide with a ring resonator: A review," IEEE Sens. J. **15**, 646–650 (2015).

[25] L. Stern, B. Desiatov, N. Mazurski, and U. Levy, "Strong coupling and high-contrast all-optical modulation in atomic cladding waveguides," Nat. Commun. **8**, 14461 (2017).
[26] R. S. El Shamy, D. Khalil, and M. A. Swillam, "Mid infrared optical gas sensor using plasmonic Mach–Zehnder interferometer," Sci. Rep. **10**, 1293 (2020).
[27] M. Giraud-Carrier, C. Hill, T. Decker, J. A. Black, H. Schmidt, and A. Hawkins, "Perforated hollow-core optical waveguides for on-chip atomic spectroscopy and gas sensing," Appl. Phys. Lett. **108**, 131105 (2016).
[28] K. T. Kaczmarek, D. J. Saunders, M. R. Sprague, W. S. Kolthammer, A. Feizpour, P. M. Ledingham, B. Brecht, E. Poem, I. A. Walmsley, and J. Nunn, "Ultrahigh and persistent optical depths of cesium in Kagomé-type hollow-core photonic crystal fibers," Opt. Lett. **40**, 5582 (2015).
[29] C. Jain, A. Braun, J. Gargiulo, B. Jang, G. Li, H. Lehmann, S. A. Maier, and M. A. Schmidt, "Hollow core light cage: Trapping light behind bars," ACS Photonics **6**, 649–658 (2019).
[30] B. Jang, J. Gargiulo, R. F. Ando, A. Lauri, S. A. Maier, and M. A. Schmidt, "Light guidance in photonic band gap guiding dual-ring light cages implemented by direct laser writing," Opt. Lett. **44**, 4016 (2019).
[31] N. M. Litchinitser, A. K. Abeeluck, C. Headley, and B. J. Eggleton, "Antiresonant reflecting photonic crystal optical waveguides," Opt. Lett. **27**, 1592 (2002).
[32] F. Davidson-Marquis, J. Gargiulo, E. Gómez-López, B. Jang , T. Kroh, C. Müller, M. Ziegler, S. A. Maier, H. Kübler, M. A. Schmidt, and O. Benson, "Coherent interaction of atoms with a beam of light confined in a light cage," Light Sci. Appl. **10**, 114 (2021).
[33] T. Barwicz, A. Janta-Polczynski, S. Takenobu, K. Watanabe, R. Langlois, Y. Taira, K. Suematsu, H. Numata, B. Peng, S. Kamlapurkar, S. Engelmann, P. Fortier, and N. Boyer, "Advances in interfacing optical fibers to nanophotonic waveguides via mechanically compliant polymer waveguides," IEEE J. Sel. Top. Quantum Electron. **26**, 1–12 (2020).
[34] A. Mekis, S. Gloeckner, G. Masini, A. Narasimha, T. Pinguet, S. Sahni, and P. De Dobbelaere, "A grating-coupler-enabled CMOS photonics platform," IEEE J. Sel. Top. Quantum Electron. **17**, 597–608 (2011).
[35] M. Nedeljkovic, J. S. Penadés, C. J. Mitchell, A. Z. Khokhar, S. Stankovic, T. D. Bucio, C. G. Littlejohns, F. Y. Gardes, and G. Z. Mashanovich, "Surface-grating-coupled low-loss Ge-on-Si rib waveguides and multimode interferometers," IEEE Photonics Technol. Lett. **27**, 1040–1043 (2015).
[36] B. Debord, A. Amsanpally, M. Chafer, A. Baz, M. Maurel, J. M. Blondy, E. Hugonnot, F. Scol, L. Vincetti, F. Gérôme, and F. Benabid, "Ultralow transmission loss in inhibited-coupling guiding hollow fibers," Optica **4**, 209 (2017).
[37] J. Bürger, J. Kim, B. Jang, J. Gargiulo, M. A. Schmidt, and S. A. Maier, "Ultrahigh-aspect-ratio light cages: Fabrication limits and tolerances of free-standing 3D nanoprinted waveguides," Opt. Mater. Express **11**, 1046–1057 (2021).
[38] A. Tuniz, C. Jain, S. Weidlich, and M. A. Schmidt, "Broadband azimuthal polarization conversion using gold nanowire enhanced step-index fiber," Opt. Lett. **41**, 448 (2016).
[39] T. P. White, B. T. Kuhlmey, R. C. McPhedran, D. Maystre, G. Renversez, C. M. de Sterke, and L. C. Botten, "Multipole method for microstructured optical fibers. I. Formulation," J. Opt. Soc. Am. B **19**, 2322 (2002).
[40] B. T. Kuhlmey, T. P. White, G. Renversez, D. Maystre, L. C. Botten, C. M. de Sterke, and R. C. McPhedran, "Multipole method for microstructured optical fibers. II. Implementation and results," J. Opt. Soc. Am. B **19**, 2331 (2002).
[41] S. Upendar, I. Allayarov, M. A. Schmidt, and T. Weiss, "Analytical mode normalization and resonant state expansion for bound and leaky modes in optical fibers—An efficient tool to model transverse disorder," Opt. Express **26**, 22536 (2018).
[42] I. Allayarov, S. Upendar, M. Schmidt, and T. Weiss, "Analytic mode normalization for the Kerr nonlinearity parameter: Prediction of nonlinear gain for leaky modes," Phys. Rev. Lett. **121**, 213905 (2018).
[43] I. Allayarov, M. A. Schmidt, and T. Weiss, "Theory of four-wave mixing for bound and leaky modes," Phys. Rev. A **101**, 043806 (2020).
[44] S. E. Braslavsky, "Glossary of terms used in photochemistry, 3rd edition (IUPAC Recommendations 2006)," Pure Appl. Chem. **79**, 293–465 (2007).
[45] B. Doherty, A. Csáki, M. Thiele, M. Zeisberger, A. Schwuchow, J. Kobelke, W. Fritzsche, and M. A. Schmidt, "Nanoparticle functionalised small-core suspended-core fibre—A novel platform for efficient sensing," Biomed. Opt. Express **8**, 790 (2017).
[46] W. L. Ng, W. R. Wong, G. Amouzad Mahdiraji, A. A. Rifat, D. C. Tee, and F. R. Mahamd Adikan, "Diamond ring fiber for evanescent field exposure," Opt. Lett. **42**, 1544 (2017).
[47] K. Sung, L. R. Brown, X. Huang, D. W. Schwenke, T. J. Lee, S. L. Coy, and K. K. Lehmann, "Extended line positions, intensities, empirical lower state energies and quantum assignments of NH_3 from 6300 to 7000 cm^{-1}," J. Quant. Spectrosc. Radiat. Transfer **113**, 1066–1083 (2012).